

# LIMEX '87 Ice Surface Characteristics: Implications for C-Band SAR Backscatter Signatures

MARK R. DRINKWATER

(Invited Paper)

**Abstract**—Ice surface characterization data collected in March 1987, during the Labrador Sea Ice Margin Experiment, are analyzed to estimate the changes in snow and ice properties at the onset of melt. Surface measurements were made from an ice research vessel on several days (some of which had coincident remote-sensing flights) at a number of locations in the marginal ice zone (MIZ). These data are used as input parameters in a simple scattering model to simulate the effects of variations in material properties upon C-band scattering signatures. Snow moisture and large-scale surface roughness are demonstrated to have the largest effect upon  $\sigma_{HH}^0$ , and large differences are predicted between undeformed floe surfaces and deformed or undulating rough ice surfaces. Using a parametric approach, an approximate picture of rough and smooth ice signatures and their relative contrast are provided. The models reproduce a trend observed in SAR images of increasing backscatter contrast between deformed and undeformed ice over an early period of warming: Such observations are consistent with the results of analysis of SAR images to date. The model also reproduces a calibrated SAR-derived signature with a reasonable degree of accuracy.

## I. INTRODUCTION

**S**URFACE properties of sea ice vary considerably both temporally and spatially, having important consequences for the backscattering and emission behavior of this polar medium. The "early melt" season marks the transition from winter conditions to warmer spring conditions, and the onset of melt is characterized by significant free water in floe surface snow. Emissivity and scattering signatures are as a result dominated by liquid water in this surface layer. In March 1987, during the pilot Labrador Ice Margin Experiment (LIMEX) [1], ice floe surface snow and sea ice were sampled at various locations in order to collect supporting ground data for several C-band Synthetic Aperture Radar (SAR) overflights [2]. These flights were conducted by the Canada Centre for Remote Sensing (CCRS) Convair-580 over a variety of study sites off the east coast of Newfoundland. Periodic measurements of snow and ice properties enabled temporal records of surface roughness, salinity, wetness, depth, and density, and photographs of the microscopic snow structure to be obtained during the onset of melt.

Various experiments and studies have been mounted over the last decade with the ultimate objective of deriving algorithms for the differentiation of ice types in radar

imagery [3]–[7]. These experiments have been limited, however, as to their geographical location and the range of frequencies and incidence angles investigated. As a result, the variation in microwave scattering properties in certain circumstances is still little understood. Experience gained from earlier campaigns has been utilized to a degree in the development of models to simulate microwave signatures of combined media [8]–[13]. Other than during the Marginal Ice Zone Experiment [14], little or no data have been collected using a C-band SAR system in a marginal ice zone during melt conditions. Sea-ice data and 5.3-GHz SAR images used in this paper provide an opportunity to apply theoretical models, developed and based upon physical/geometrical optics approaches, to marginal ice surfaces examined in the Grand Banks region of the Labrador Sea under warming conditions. Models are driven using physical properties measured *in situ* and are used to explain the range of scattering signatures of targets observed in the radar images.

## II. LIMEX '87 SURFACE OBSERVATIONS

Sea-ice conditions were monitored throughout LIMEX between March 15 and 26, 1987 off the east coast of Newfoundland [1], [2]. Detailed surface data were collected on several days, concurrently with remote-sensing overflights, in order to characterize surface conditions and identify changes in material properties. The geographical locations of experiment surface sites are shown in Fig. 1, and the position of the ice edge is included to indicate the zones within the marginal ice where measurements were conducted.

### A. Measured Snow and Ice Properties

Parameters recorded in the field by the surface data team included snow and ice depths, and snow salinity, wetness, density, and temperature. Two-dimensional profiles of the snow surface were obtained with the aid of a roughness profiler, and the author also obtained macrophotographs of snow-grain morphology (at 10X magnification).

Sea-ice cores were extracted in several locations using the Centre for Cold Oceans Resource Engineering (C-CORE) equipment. Core lengths were cut into 5- and 10-cm sections and allowed to thaw. The salinity of samples was determined with an Endeco optical salinometer calibrated at room temperature.

In addition to snow and ice surface characteristics, local meteorological conditions were monitored during the

Manuscript received December 20, 1988; revised February 19, 1989. This work was supported by a National Research Council Research Associateship.

The author is with the Jet Propulsion Laboratory, California Institute of Technology, 4800 Oak Grove Drive, Pasadena, CA 91109.  
IEEE Log Number 8928696.

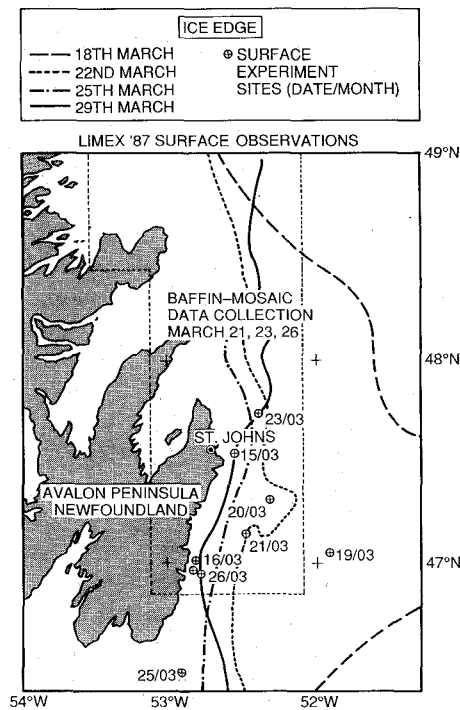


Fig. 1. LIMEX '87 surface experiment sites and extent of the marginal ice zone. The dotted rectangle delineates the area within which coincident aircraft SAR flights were made in order to create image mosaics on March 21, 23, and 26 of sea ice in the CSS *Baffin* locality.

course of observations at each experimental site; an automated weather station located on the vessel CSS *Baffin* also continuously recorded a variety of parameters. Six hourly averages of winds recorded at St. John's, mean winds recorded during surface measurements on the ice, and shipborne winds in periods when the ship was stationary are synthesized in Fig. 2(a). The accompanying air temperature trace in Fig. 2(b) indicates that warm and cold periods are synchronized with the wind direction. Melting conditions are induced by warm, moist southeasterly winds, while subzero refreezing conditions occur during bouts of predominantly northeasterlies.

1) *March 16*: Surface experiments were carried out while the CSS *Baffin* was in the interior MIZ. A deep snow layer of mean depth 16 cm was recorded on top of relatively undeformed sea ice after a recent heavy snowfall (on March 13). Snow stratigraphy records and density measurements are described in Fig. 2(c). Snow crystal macrophotographs indicate that the snow layer was being transformed by the processes of grain rounding and sintering. For a month prior to the experiment, temperatures recorded at St. John's were predominantly below freezing (i.e.,  $0^{\circ}\text{C}$ ). Under cold conditions, the process of "equi-temperature metamorphism" [15] begins immediately after precipitation, rapidly changing the characteristics of the snow layer deposited on sea-ice surfaces. Characteristics distinguishing the onset of this type of destructive metamorphism are the transformation of original snow crystal forms and the production of uniform well-rounded grains without any remaining angular crystal facets [15]. As temperatures rose above freezing on March 15,

metamorphic processes responded to temperatures fluctuating around freezing for 24 h prior to the first surface observations. Fig. 3 illustrates a snow sample from a 4-cm depth, and the well-rounded 1-mm diam grains and bonded grain necks indicate the melt-freeze metamorphism of the snow layer. Such snow, with clusters of rounded ice grains, is commonly known as "corn snow" [15]. The upper part of the layer was dampened by snow meltwater, while the basal layer was relatively wet due to gravity percolation down to the snow/ice interface. The mean recorded snow density was  $450\text{ kg m}^{-3}$  at this location.

2) *March 20*: A typical snow profile obtained on this day contained the attributes displayed in Fig. 2(c). Snow depths varied from zero to a maximum depth of 15 cm, but cycles in the temperature and accompanying melt-freeze had reduced the mean snow depth to 12 cm. Snow crystals had suffered from the effects of the raised temperatures (Fig. 2(b)) and had been transformed via the process of melt-freeze metamorphism [15]. Under these conditions, smaller ice grains in the surface layer melt during warmer periods. The resulting meltwater percolates into the snow and the layer becomes a two-phase mixture. During periods of refreezing, free water trapped between ice crystals and in pore spaces forms grain necks, fusing or bonding snow crystals together into polycrystalline aggregates of larger grains. This snow is classified on the basis of the snow crystal macrophotographs and categorized as "advanced firn snow" [16].

Snow densities had increased and two distinct layers developed; the upper had a mean density of  $480\text{ kg m}^{-3}$ , and the lower a mean density of  $500\text{ kg m}^{-3}$ . The former had well-rounded grains with a mean diameter of 1.2 mm bonded by meltwater refrozen between grain necks. The latter was wetter, having large grains of 3-mm mean diam formed of clusters of small, round ice crystals.

3) *March 21*: Stratigraphic data demonstrated the characteristics in Fig. 2(c). Freezing overnight temperatures below zero resulted in a surface crust. As morning progressed, ambient air temperatures increased (Fig. 2(b)) and the surface snow warmed. Mean snow temperatures of approximately  $0^{\circ}\text{C}$  led to grain necks thawing and snow pore spaces becoming occupied by water. The snow became friable as bonds of aggregated grains disintegrated. Beneath a surface crust, the shallow snow layer (approx. 4-cm depth) was granular, with a mean density of  $500\text{ kg m}^{-3}$ . Photographs taken of ice surface morphology indicate that by this date large proportions of ice floe surfaces had become particularly well deformed.

4) *March 25*: The surface snow layer had increased in density to the extent that it was no longer possible to obtain representative samples of structure. Recrystallization had transformed snow into advanced firn [16] in a thin white opaque layer to a depth of 2 or 3 cm upon the surface of the ice (Fig. 2(c)). Repeated melt-freeze cycles enabled an appreciable gain in density of the surface layer and an increased mechanical strength. The typical density range of snow in this category is  $600\text{--}700\text{ kg m}^{-3}$ . Fig. 4

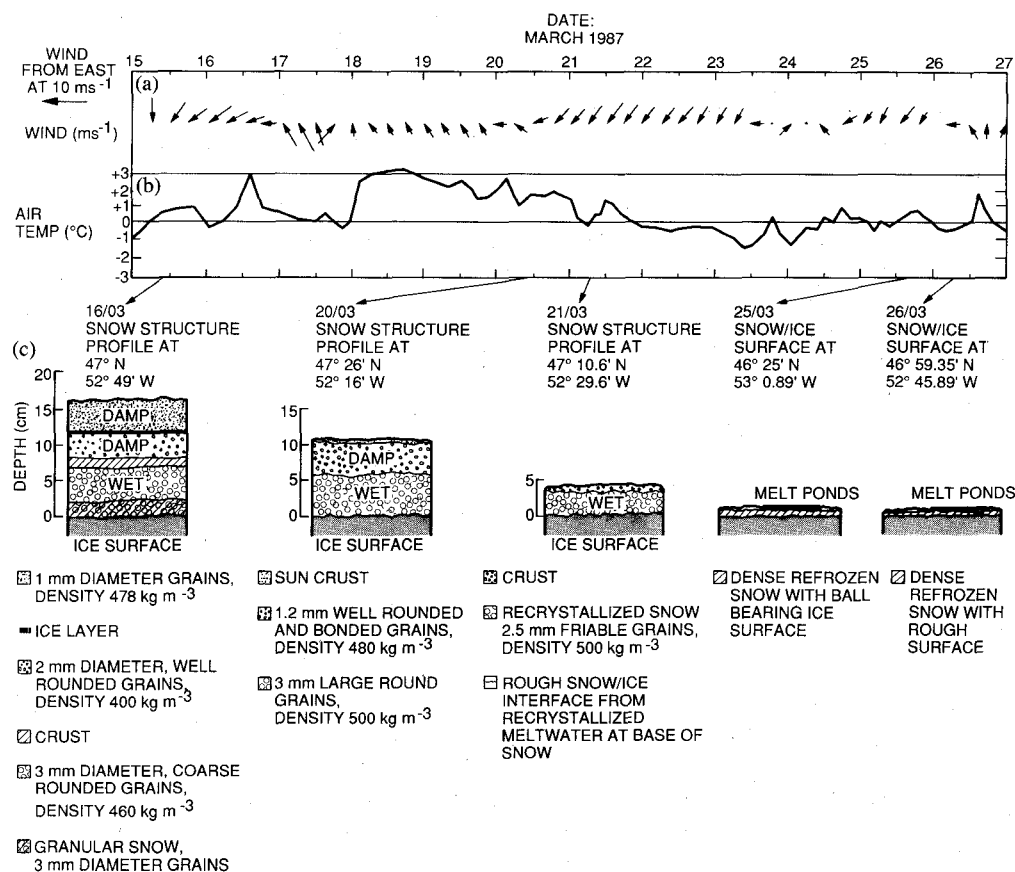


Fig. 2. Meteorological and ice surface conditions during the LIMEX '87 experiment period. (a) Indicates the wind speed and direction, (b) shows the corresponding temperatures, and (c) describes typical surface conditions at particular locations, in terms of the snow structure, crystal morphology, and density.



Fig. 3. A snow crystal macrophotograph at approximately 10X magnification taken on March 16. It shows a tightly packed cluster of rounded melt-freeze grains with diameters of around 1 mm.

shows small-scale surface roughness formed by aggregates of large ice crystals around the rims of floes.

5) *March 26:* On the final day of surface data collection, surveys were conducted at three individual sites along a transect orthogonal to the ice edge. The mean depth of the dense firm remaining on ice floe surfaces was 2 cm, though many had melt pools in areas where this layer had melted (Fig. 2(c)). Macrophotographs indicate that the firm was aggregated into large tightly packed clus-

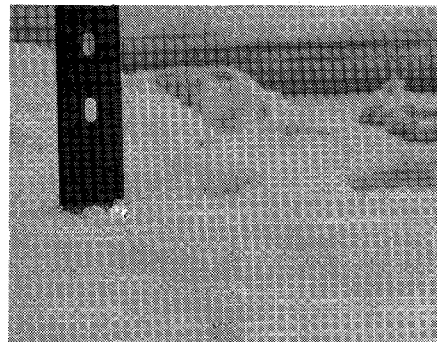


Fig. 4. Surface clusters of "ball-bearing ice" with large cm-scale interlocking grains found around the rims of ice floes, taken on March 25.

ters of large (2.5–3-mm diam) well-rounded grains, which was given the descriptive term "ball-bearing ice."

Patches of bare blue sea ice were observed on many ice floes by this stage in the experiment. Most floes had levées and had been further deformed and fractured by collisions and rafting under pressure in the MIZ. However, large rafted blocks and pressure ridges were no longer evident owing to the advance or the limit of wave action and the disintegration of large piles or upstanding chunks of ice. Few floes had substantial areas of flat surface exposed to the aircraft SAR.

### B. Overview of Surface Properties

Surface snow decreased rapidly in depth throughout the course of the experiment (Fig. 2(c)). Snow crystal macro-photographs illustrate that the collective processes of destructive metamorphism changed the medium into a variety of stages of "firm" [16]. What was observed between March 16 and 26, therefore, was a continuum of states between the beginning of snow metamorphosis and the formation of higher-density polycrystalline ice. By March 26, the top few centimeters of the surface had become a near-continuous layer of snow ice, almost like freshwater ice.

### III. SNOW MELT AND ICE SURFACE DESALINATION

Surface characterization data show that melt-freeze cycles and melt drainage ultimately reduced the surface snow layer to a near-zero depth in most locations. Ice cores were extracted in several locations, and Fig. 5 describes the mean salinity profiles from ice sampled on March 23 and 26. These indicate that significant desalination had occurred in the upper ice layer (0–30 cm) as a likely consequence of brine drainage channel development and flushing by snow meltwater during warm periods. In the upper 10 cm, salinity values typically range from 0–2.0‰. For March 26, a strong salinity gradient is observed down between 25 and 35 cm, and a maximum salinity of 8‰ was measured at a 35-cm depth in one core. Below 35 cm, the mean salinity remains reasonably constant in both profiles, remaining between 3 and 5‰ down to 115 cm.

Ice in the interval 35–110 cm shows a reasonably stable salinity, seemingly unaffected by the onset of desalination processes, and appears to indicate original bulk salinities of between 4–5‰. These characteristics appear to be consistent with measurements of first-year fast ice desalination made in Mould Bay during June and July 1982 [17]. Flushing seems the most probable mechanism behind rapid desalination, due to the large amount of surface meltwater produced by snow-layer thaw. Flushing occurs under gravity drainage as the pressure head of surface meltwater overcomes the capillary retention of brine in pockets within the ice. Providing that the ice is permeable, meltwater is able to penetrate and drain downwards [18], [19]. Mean ice thicknesses in the core localities were 2.7 and 1.6 m on March 23 and 26, respectively. This indicates that rafting was of particular importance in augmenting ice thickness and perhaps in initiating the onset of desalination by uplifting and increasing the freeboard of the ice and the resulting pressure head. This factor would explain the lower bulk salinities observed in the profile for March 23 in Fig. 5.

### IV. DIELECTRIC PROPERTIES OF OBSERVED MEDIA

#### A. The Complex Dielectric Properties of Wet Snow

Wet-snow permittivity ( $\epsilon'$ ) and dielectric loss ( $\epsilon''$ ) are frequency dependent, showing large increases with liquid water content in the GHz range. Both Colbeck [20] and

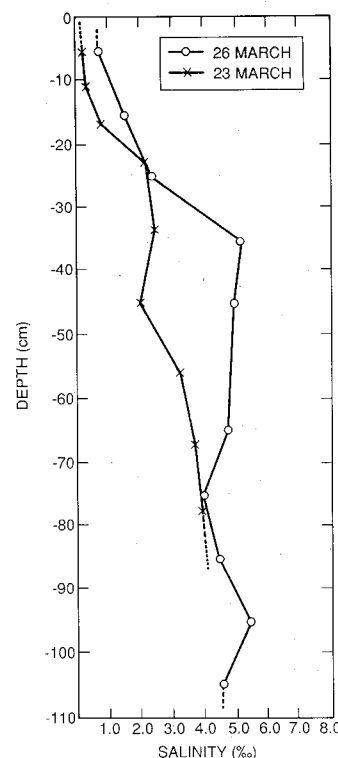


Fig. 5. Mean salinity profiles obtained from ice cores taken on March 23 and 26 and sampled at 10-cm intervals.

Tiuri *et al.* [21] investigated the dependence of the complex dielectric constant ( $\epsilon^*$ ) of snow upon grain structure, wetness, and frequency (where  $\epsilon^* = \epsilon' - j\epsilon''$ ). At microwave frequencies close to the relaxation frequency of water, such as 5.3 GHz,  $\epsilon'$  and  $\epsilon''$  become almost independent of the snow structure. Instead, according to [21], water dominates the behavior of the real and imaginary parts of  $\epsilon^*$ . In fact, the effective relaxation frequency ( $f_0$ ) of undisturbed wet snow (i.e., the frequency at which  $\epsilon''$  has its maximum value) is found consistently at  $10 \pm 1$  GHz [22], [23] at a temperature of 0°C. Loeb *et al.* [24] observe a relaxation frequency of 11 GHz in pure water at 5°C, and so it is concluded that the dielectric properties of wet-snow mixtures depend significantly upon the relaxation spectrum of water.

Tiuri *et al.* [21] utilize the Taylor dielectric mixture formula [25] to consider a combination of air and water between ice particles. Water inclusions are assumed to conform to a shape halfway between randomly oriented needle-like shapes and spheroids, as this is close to what has been observed in reality. The empirical relationship used to find the permittivity of a known density ( $\rho_{\text{dry}}$ ) of dry snow excluding any water (from [21]) is

$$\epsilon'_{\text{dry}} = 1 + 1.7\rho_{\text{dry}} + 0.7\rho_{\text{dry}}^2 \quad (1)$$

where  $\rho$  is measured in  $\text{g cm}^{-3}$ . The increase in the permittivity of the snow by a small amount  $\Delta\epsilon'_{\text{wet}}$ , when water is included, is simply

$$\Delta\epsilon'_{\text{wet}} = \epsilon'_{\text{wet}} - \epsilon'_{\text{dry}} \quad (2)$$

Tiuri *et al.* find a pair of expressions to calculate the permittivity and dielectric loss of wet snow in the GHz frequency range [21], given (1) and (2):

$$\Delta\epsilon'_{\text{wet}} = \epsilon'_w(0.1W_v + 0.8W_v^2) \quad (3)$$

$$\epsilon''_{\text{wet}} = \epsilon''_w(0.1W_v + 0.8W_v^2). \quad (4)$$

$W_v$  is the volume fraction of water, and the relative permittivity ( $\epsilon'_w$ ) and dielectric loss ( $\epsilon''_w$ ) of water are calculated for 5.3 GHz as 65.8 and 36.51, respectively, using a simple Debye equation [21]. Fig. 6 shows the results of calculating of  $\epsilon'_{\text{wet}}$  and  $\epsilon''_{\text{wet}}$  by using (1)–(4) with varying  $W_v$ . The value of  $\epsilon''_{\text{wet}}$  tends to zero for snow with no free water, but increases rapidly as water is included.  $\epsilon'_{\text{wet}}$  also responds, increasing by about 1.9 with the addition of 15 percent water by volume fraction. The response of  $\epsilon'_{\text{wet}}$  to snow density ( $\rho_s$ ) is also included for the three snow densities, 200, 400, and 600 kg m<sup>-3</sup>, illustrating that increases in permittivity are proportional to density increases.

Caution is required in extracting values from Fig. 6, as (3) and (4) are derived for old coarse snow in the “pendular regime” (i.e., less than 14 percent of pore volume filled with water [20]). This state occurs when the snow-water volume fractions are still low enough for water to be held at the necks between snow-grain boundaries. Variability in  $\epsilon'_{\text{wet}}$  and  $\epsilon''_{\text{wet}}$  increases when snow crosses the transition from the pendular to the funicular regime (where drainage begins), and so these two regimes are delineated by shading in Fig. 6 for  $\epsilon'_{\text{wet}}$  at each density. For snow of 400 kg m<sup>-3</sup>, in transition between the two regimes,  $\epsilon'$  and  $\epsilon''$  are estimated to be at 2.65 and 0.5.

Snow wetness measurements were made on March 20 using the dye dilution technique [26]. The accuracy of these measurements relies on the temperature of a given dye solution being 0°C when introduced to a snow sample, otherwise the snow crystals begin to melt. Since many of the recorded measurements were obtained at temperatures above zero, the reliability of the majority of estimates cannot be trusted. However, those few obtained (at temperatures close to freezing) from the damp surface snow layer shown in Fig. 2(c) gave an estimate of a liquid mass volume fraction of about 0.22. When corrected for locally measured snow densities ranging between 400 and 500 kg m<sup>-3</sup>, these data indicate an approximate range of  $W_v$  between 0.08 and 0.11 (i.e., between 8 and 11 percent by volume). Thus, on March 20 the upper snow layer was in transition between the pendular and funicular regimes.

Given the observed parameters, it is evident that the surface firm and its variations in water content (and to a lesser extent density and ice-crystal morphology) govern the dielectric properties of floe surfaces. A damp, shallow snow layer attenuates microwave energy and modifies the response of the snow/ice interface and the sea ice beneath [27]. Thus, the varying depth and water content of this layer will bear a large degree of influence upon the microwave scattering properties of ice floe surfaces.

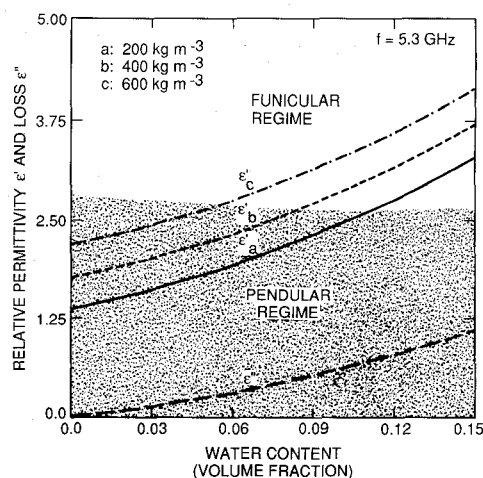


Fig. 6. The dielectric properties of wet snow at a frequency of 5.3 GHz. The permittivity and dielectric loss are plotted for varying snow-water content and densities of 200, 400, and 600 kg m<sup>-3</sup>. The shaded region indicates the value of  $\epsilon'_{\text{wet}}$  for snow of given density and wetness in the pendular regime.

### B. Microwave Dielectric Properties of Labrador Sea Ice

The dielectric properties of first-year Arctic sea ice are well documented. Vant *et al.* [28] and Arcone *et al.* [29] investigated the complex dielectric properties of ice with salinities between 3 and 10‰ in the frequency range 0.1–40 GHz. Recently, Drinkwater and Crocker [13] theoretically modeled dielectric properties of high-salinity first-year ice at microwave frequencies using measurements of properties of young fast ice in the Canadian Arctic. To complete the range of microwave dielectric properties, Hallikainen *et al.* [22] made a series of measurements of low-salinity ice in the Gulf of Bothnia during April 1987. Importantly, their dielectric measurements of warm first-year sea ice under melting conditions (−6.0° to −0.3°C) cover the remaining unknown low-salinity range between 0 and 1.0‰. These measurements indicate electromagnetic properties of ice most comparable with extensively desalinated ice observed in the Labrador Sea. Since  $\epsilon^*$  is most closely linked to the volume fraction of liquid brine, it is important to know the effects of desalination upon the complex dielectrics of the ice medium. Hallikainen *et al.* [22] observe that as the low-salinity ice is warmed to temperatures between −1° and 0°C, the volume fraction of brine in the ice rapidly reaches a maximum. The consequence for ice in the salinity range 0.7–0.9‰ is an increasing permittivity and dielectric loss from levels more typically associated with pure ice ( $\epsilon^* = 3.1 - j0.01$ ) at −2°C to values around  $\epsilon^* = 4.3 - j1.0$  at a temperature of −0.2°C.

### C. C-Band Penetration Depth in Labrador Sea Marginal Ice Surface Media

As explained, the snow layer and its liquid water content increase losses, generally making the underlying ice less significant in the backscattering process. Even a small depth of wet snow can mask the response from the sea ice

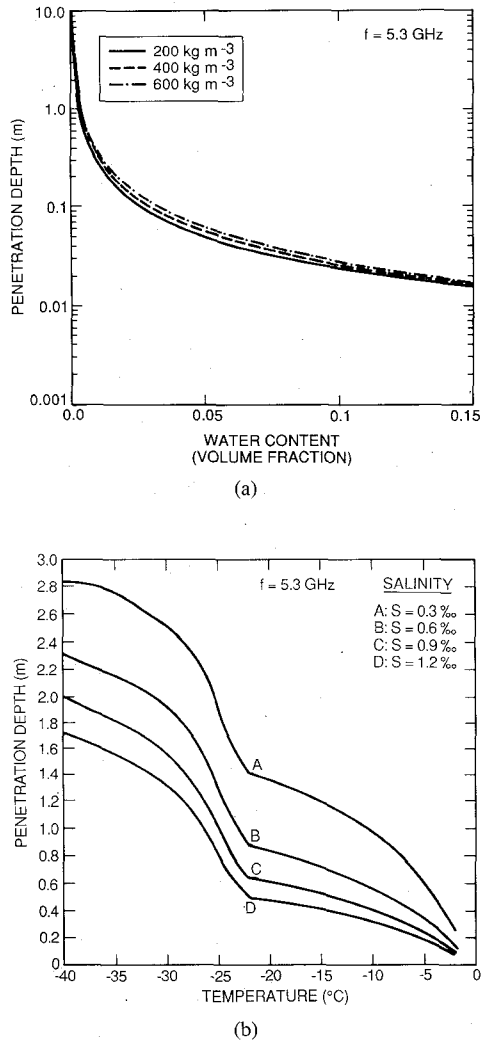


Fig. 7. The predicted penetration depth of C-band microwave energy in (a) snow of a known volume fraction of pure water. The three curves indicate that snow density has little effect upon  $\delta_p$  in the range plotted. (b) Shows  $\delta_p$  in low salinity columnar sea ice of density 850 kg m<sup>-3</sup>. Curves A-D indicate significant reductions in  $\delta_p$  with increasing salinity and temperature.

by attenuating energy sufficiently rapidly such as to enable only shallow penetration [27] into the surface layer. The penetration depth  $\delta_p$  in a wet snow or sea-ice medium is controlled by the scattering and absorption losses due to the mixture of dielectrics and material structure. If scattering losses are assumed to be negligible,  $\delta_p$  is [30]

$$\delta_p = \frac{\lambda}{4\pi} \left\{ \left[ \left( 1 + \left( \frac{\epsilon''}{\epsilon'} \right)^2 \right)^{1/2} - 1 \right] \frac{\epsilon'}{2} \right\}^{-1/2} \quad (5)$$

where  $\lambda$  is the wavelength,  $\epsilon'$  is the permittivity of the medium, and  $\epsilon''$  is the dielectric loss of the medium. In Fig. 7(a) penetration depth curves are calculated for wet snow with various densities at 5.3 GHz, using (1)–(5). The curves demonstrate that  $\delta_p$  is reduced dramatically with the addition of small amounts of water, and using this approximation appears to be insensitive to the density of the snow. With 10 percent water by volume fraction,  $\delta_p$  is reduced from the order of several meters to between

0.02 and 0.03 m, corresponding well with the results in [14].

Late in the experiment, when the firm is shallow, the underlying low-salinity ice surface can contribute to the backscatter signature of the radar. Fig. 7(b) illustrates the temperature and salinity dependence of  $\delta_p$  in columnar first-year ice at 5.3 GHz (after [12]). A characteristic kink occurs at  $-22.9^\circ\text{C}$  due to the temperature, salinity, and brine volume phase relations for sea ice [31]–[33]. Importantly, however, during LIMEX '87 the upper ice interface temperature was never lower than  $-3^\circ\text{C}$  and remained close to  $0^\circ\text{C}$  throughout this period. Curves in Fig. 7(b) show that  $\delta_p$  tends rapidly to zero for ice of any salinity in the temperature range  $-5^\circ$  to  $0^\circ\text{C}$ . This demonstrates that volume scattering within the sea ice may effectively be disregarded.

## V. SURFACE ROUGHNESS AND RADAR BACKSCATTERING

When snow is wet,  $\delta_p$  is small and the surface roughness becomes of major importance in influencing microwave signatures [30], [34], and [35]. The relationship between surface roughness and surface scattering is well understood [36]. In the context of SAR imagery, a flat specular sea-ice surface reflects incident energy away from the antenna, resulting in the target area appearing dark. With a relatively rough surface, some energy may be backscattered to the antenna, resulting in a bright target area.

### A. Surface Roughness Measurements

Several roughness profiles were obtained of snow and ice surfaces. The apparatus and technique used enabled the height of discrete elements of a surface profile to be measured. Sampling was possible at 1-cm intervals in 1-m sections along a transect. Statistics derived using this technique have been analyzed numerically. The degree of roughness of these surface sites is quantified in terms of the standard deviation ( $\sigma$ ) of surface height elements (or rms height) and the surface autocorrelation function-derived correlation length ( $l$ ). Since variations in surface height are assumed to be random, the mean surface is used as a reference level. Values of  $\sigma$  and  $l$  describe the statistical variation of the *random* component of surface height relative to the reference surface [36].

Normalized autocorrelation functions are derived from the statistics, where  $p(x')$  is a measure of the similarity between two height elements separated by a given distance  $x'$ , where  $x' = (\text{lag} - 1) \Delta x$ , and  $\Delta x$  is the spatial sampling interval in the horizontal direction. The lag is an integer where  $\text{lag} > 0$  and whose maximum value is limited by the length of the sampled profile. The correlation length ( $l$ ) is derived from the normalized autocorrelation function, being defined as the displacement at which  $p(x') = 1/e$  ( $\approx 0.37$ ) [36]. The statistic  $p(x')$  provides a measure of the dependence of closely separated points upon a surface profile. If  $x' \leq l$ , then their heights are statistically dependent upon one another, and if  $x' > l$  they are considered to be statistically independent.

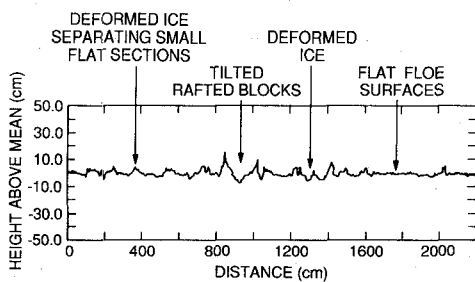


Fig. 8. Surface profile obtained from roughness measurements made along a 22-m transect. The profile indicates cm-scale roughness in both undeformed and deformed ice areas.

One drawback realized from this measurement strategy is that optimally  $\Delta x \leq \lambda/10$  to ensure that surface segments have no appreciable effect upon scattering from the surface. In this case  $\Delta x \approx \lambda/5$  at the SAR frequency of 5.3 GHz. Notwithstanding this deficiency, statistics presented in the following section indicate that larger-scale surface roughness elements are likely to be dominant in the effect of slope profile facets upon scattering, and the sampling strategy is unlikely to be to the detriment of the overall results.

### B. Surface Profile Statistics

A surface profile from a 22-m co-registered section of a transect obtained on March 20 is shown in Fig. 8. Statistics extracted from this profile indicate that height elements are normally distributed around the mean (or reference level), approximating a Gaussian distribution. The standard deviation  $\sigma = 2.72$  cm and the rms slope  $s = 0.33$  rad ( $\sim 19^\circ$ ) and the form of the distribution and high rms slope are influenced by the overall degree of deformation of this marginal ice. Rubbled floe edges and rafting caused by extreme pressure conditions [37] are responsible for the undulations of the order of a 10- or 15-cm amplitude in Fig. 8.

## VI. SURFACE AND SUBSURFACE SCATTERING CONTRIBUTIONS FROM A COMPOSITE MARGINAL ICE ZONE

### A. Surface Roughness Components

Fig. 9 illustrates autocorrelation statistics for the two roughness classes identified from field data. Solid curves in Fig. 9(a) and (b) are representative of the autocorrelation functions of deformed, rafted or rubbled areas, and flat floe surfaces, respectively. For rougher profile sections in Fig. 9(a), the standard deviation  $\sigma = 4.43$  cm. In contrast, statistics in Fig. 9(b) are from smoother sections (see Fig. 8, that has a distance of 17 m), and  $\sigma = 1.74$  cm. Other important statistics derived from the surface profile sections used for Fig. 9(a) and (b) are rms slopes of 0.38 and 0.23 rad, and correlation lengths  $l = 18.6$  and  $l = 12.8$  cm, respectively.

Though rough deformed ice was sampled in order to obtain the statistics shown in Fig. 9(a), the majority of rough ice circumstances were either inaccessible or impossible to sample using the technique described. Statis-

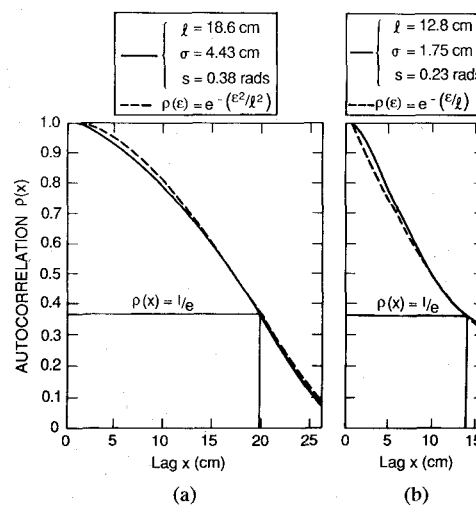


Fig. 9. Autocorrelation functions for ice in (a) deformed areas, and (b) undeformed, relatively flat floe surfaces. Solid lines indicate measured curves along with respective surface correlation length ( $l$ ), standard deviation ( $\sigma$ ) of surface roughness, and rms slope ( $s$ ). Dashed lines indicate closely corresponding autocorrelation curves for ideal surfaces with (a) a Gaussian, and (b) an exponential probability distribution as a function of height ( $\epsilon$ ) and  $l$ .

tics derived should only be used with the caveat that these data are not representative of the large-scale roughness elements such as pressure ridges and the large rubble piles observed in active zones of ice shear. The maximum observed rms slope, for instance, was only 0.5 rad, and since the bias is towards the higher end of the roughness spectrum, it is expected that in reality locally rough areas such as pressure ridge ice piles can have rms slopes as great as 0.8 rad (or  $45^\circ$ ).

It is evident from photography and the properties and statistics extracted from surface profiles that the MIZ is composed largely of rubbled or deformed ice separated by areas of undeformed, relatively flat, desalinated first-year ice. It is suggested that without a composite scattering formula, no single scattering approximation can be used to represent the scattering properties of this composite MIZ surface. Various scattering formulations have been used to approximate the backscatter response in given circumstances, however. Plotted alongside in Fig. 9(a) and (b) are dashed Gaussian and exponential autocorrelation functions, which indicate that the curves can be represented by simple functions to a first approximation. Thus, providing that the criteria for applicability are met regarding surface roughness, the scattering response from these two distinct surface classes may be predicted with simple Kirchhoff scattering formulae previously derived by Barick [39] and Eom [38] using similar Gaussian and exponential approximations.

### B. The Kirchhoff or Physical Optics Surface-Scattering Formulation

Among the many theories for surface scattering, the Kirchhoff or physical optics formulation is one of the most widely used [8], [39]–[41]. It is applicable to surfaces with undulations whose average horizontal dimensions are



large with respect to the incident wavelength. The main restriction under which its simplifying assumptions are valid is that the average radius of curvature  $\vartheta_c > \lambda$ . For an autocorrelation function approximating to a Gaussian distribution, as with the rougher of the two surfaces,  $\vartheta_c$  is defined as [36]

$$\vartheta_c = l^2 / 2.76\sigma. \quad (6)$$

An additional restriction is that the correlation length, or horizontal-scale roughness  $l$ , is larger than one wavelength, and that

$$k_0 l > 6 \quad (7)$$

where  $k_0 = 2\pi/\lambda$ .

Given the statistics in Figs. 9(a) and 10(b) for the two broad surface-roughness classes, these criteria are met. In these cases, the Kirchhoff surface integral is further simplified using two approximations, one for surfaces with  $s < 0.25$  rad, and the other for rougher surfaces with  $s > 0.25$  rad [36]. The former is a "scalar approximation" and is applicable when  $\sigma$  is a fraction of  $\lambda$ , as is the case of the surface segment used for Fig. 9(b). The alternative for a rough surface, described by the autocorrelation function in Fig. 9(a), is a simple geometric optics formulation with a "stationary-phase approximation" [42].

### C. Scalar Approximation for Smooth-Surface Backscattering

The scalar approximation is used here to calculate the range of backscattering coefficient ( $\sigma^0$ ) for undeformed ice. Previously, this technique has been used to reproduce the scattering signature of first-year ice with an exponential autocorrelation function [9], [10]. The requirements for this model are satisfied for surfaces with similar statistics to the profile used for Fig. 9(b), at a frequency of 5.3 GHz. Using a correlation function of the form

$$p(\xi) = \exp\left(-\frac{\xi}{l}\right) \quad (8)$$

the following expression for the  $HH$  polarized backscatter coefficient is derived [38]:

$$\sigma_{HH}^0(\theta) = 2 |\Gamma_{HH}|^2 \cos^2 \theta \exp(-4k_0^2 \sigma^2 \cos^2 \theta) \cdot \sum_{n=1}^{\infty} \frac{(4k_0^2 \sigma^2 \cos^2 \theta)^n}{n!} \frac{(k_0^2 n/l)}{(4k_0^2 \sin^2 \theta + n^2/l^2)^{3/2}} \quad (9)$$

where  $HH$  is the polarization,  $\Gamma_{HH}$  is the Fresnel reflexion coefficient, and  $\theta$  is the incidence angle.

### D. Stationary-Phase Approximation for Rough-Surface Backscattering

For rough or deformed ice surfaces a geometric optics model [39] is more appropriate. Such a formulation is widely used and discussed in [36] and [43] for a Gaussian correlation function. The model parameters required are simply the  $HH$  polarized Fresnel reflexion coefficient

$\Gamma_{HH}(0)$  at normal incidence and the unidirectional rms surface slope  $s$ .

The approximation is valid providing  $k_0 \sigma > 2$  and  $\sigma > \lambda/3$  [36]. For the field observations of  $\sigma = 4.4$  cm and larger on deformed ice surfaces, these conditions are satisfied. The formula, however, does not account for multiple scattering, and so depolarization effects are ignored. The backscatter coefficient  $\sigma^0$  comprises noncoherent  $HH$  polarized surface scatter and is a function of surface slope and incidence angle. It is also independent of the surface autocorrelation function.

### E. Volume Scattering from the Snow Layer

Volume scattering from the snow layer depends primarily upon the amount of energy transmitted into the medium and the effective penetration depth  $\delta_p$ . Even for wet snow, over 90 percent of the incident energy is transmitted across a smooth air/snow interface (when  $\Gamma_{HH}(0) < 0.28$ ). At the start of the experiment, snow wetness values estimated at  $W_v = 0.05$  or less mean that  $\delta_p$  is sufficiently large so that several centimeters of the snow volume contribute to volume scattering. Backscattering takes place from ice grains and free-water inclusions, and the intensity of volume scatter is governed by their size and dielectric properties and the losses occurring by extinction within the layer. The total volume-scattering coefficient is calculated by summing the individual backscatter components from ice grains and water inclusions, where  $N_1$  is the number density or number of ice scatterers per unit volume ( $m^{-3}$ ) and  $N_2$  is the number density of water inclusions. Since these scatterers are small relative to the wavelength, the "Rayleigh approximation" [44] is used to calculate the backscatter cross section of an individual particle. If scatterers are assumed to be spherical, the backscatter cross section  $\sigma_b$  is [45]

$$\sigma_b = \frac{64\pi^5 r^6}{\lambda_0^4} |K|^2 \quad (10)$$

where  $r$  is the radius of the scatterer,  $\lambda_0$  is the free-space wavelength, and  $K$  is a complex quantity defined in terms of the complex dielectric constant of the particle  $\epsilon_p^*$  relative to the background medium  $\epsilon_m^*$ , where

$$|K|^2 = \left| \frac{(\epsilon_p^* - \epsilon_m^*)}{(\epsilon_p^* + 2\epsilon_m^*)} \right|^2 \quad (11)$$

Number densities or the relative numbers of ice or water particles per unit volume may be calculated from

$$N = 3\nu/4\pi r^3 \quad (12)$$

where  $\nu$  is the volume fraction of either ice or water. The total volume-scattering coefficient  $\sigma_v$  is then given by

$$\sigma_v = N_1 \sigma_{b1} + N_2 \sigma_{b2}. \quad (13)$$

The backscattering coefficient from the snow volume is then expressed as [36], [13]

$$\sigma_v^0 = \frac{\sigma_v \cos \theta'}{2k_e} \left( 1 - \frac{1}{L^2(\theta')} \right) \quad (14)$$



where  $k_e = 1/\delta_p$ ,  $\theta'$  is the transmission or refraction angle, and the one-way loss factor  $L(\theta')$  in snow of depth  $d$  meters is

$$L(\theta') = \exp(k_e d \sec \theta'). \quad (15)$$

#### F. Combined Backscatter Coefficient $\sigma^0$

Both the surface scattering contribution  $\sigma_s^0$  and the snow volume-scatter contribution  $\sigma_v^0$  must be combined in order to calculate the total backscatter coefficient  $\sigma_{\text{total}}^0$  from ice floe surfaces. Clearly, calculations of  $\delta_p$  for wet snow indicate that a negligible portion of energy penetrates deep enough for the sea-ice medium beneath to contribute to overall backscatter totals. Additional attenuation within the wet snow layer means that sea-ice volume backscatter can effectively be ignored under these circumstances. Thus,  $\sigma_s^0$  and  $\sigma_v^0$  are summed:

$$\sigma_{\text{total}}^0(\theta) = \sigma_s^0(\theta) + T_{\text{as}}^2(\theta')(\sigma_v^0(\theta')) \quad (16)$$

and the transmission coefficient at the air/snow interface  $T_{\text{as}} = (1 - \Gamma_{\text{HH}})$ .

### VII. COMBINED MODEL RESULTS

#### A. Undeformed Ice Floe Surfaces

The scattering signature of undeformed ice floe surfaces are simulated using the assumption of an exponential surface correlation function. Mean values of field-measured parameters such as snow density are used to drive the model, and the five combinations of values listed in Table I give a scattering signature for each surface described in Fig. 2(c). Predicted signatures in Fig. 10 for floes without changes in surface roughness indicate that as snow density and volume fraction of liquid water increase, the gradient of  $\sigma^0$  in the incidence range  $40^\circ < \theta < 80^\circ$  increases. This result concurs with expected reductions in volume scatter and a larger portion of incident energy reflected away from the radar at the snow surface [27]. In using the measured snow parameters (Table I) and surface roughness properties from Fig. 9(b), the level of the curves does not vary by more than 2–3 dB. Yet it is evident from previous investigations with images such as Fig. 11, obtained during the height of the melting period (March 18–22), that certain floes appear much darker than their surrounding counterparts [46], taking on an image intensity almost as low as open-water areas. None of the combinations of surface parameters account for standing water or a saturated upper layer upon ice floes (as indicated in Fig. 2(c)), and so an additional curve is plotted in Fig. 10 to represent the signature of the saturated floes observed on March 25 and 26. Wet snow surface dielectric conditions used to generate this signature were  $\epsilon_{\text{snow}}^* = 4.3 - j1.0$ , along with the roughness statistics for the smoothest surface observed ( $\sigma = 0.73$  and  $l = 7.0$  cm). This signature, in contrast, shows a marked reduction in  $\sigma^0$  throughout the incidence angle range of between 4 and 12 dB. It demonstrates that saturated or flooded floes may be expected to have relatively lower backscatter val-

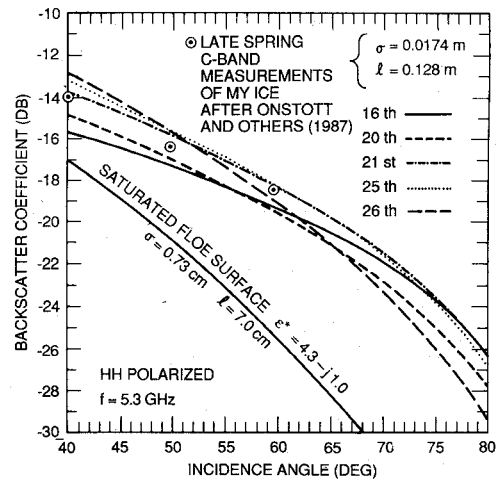


Fig. 10. Simulated C-band *HH* polarized scattering signatures for each of the five days, using parameters listed in Table I and given roughness statistics for an undeformed exponential surface. Scatterometer data points recorded over spring multiyear (MY) ice are indicated, and a signature predicted for smooth saturated floe surfaces is included for contrast.

TABLE I  
PARAMETERS USED IN MODELING FLOE SURFACE RESPONSE THROUGHOUT THE LIMEX EXPERIMENT (MARCH 16–26)

Snow Property	16/03	20/03	21/03	25/03	26/03
$r_{\text{snow}}$ (m)	0.001	0.0011	0.00125	0.00125	0.00125
$W_v$	0.05	0.09	0.11	0.11	0.15
$d_{\text{snow}}$ (m)	0.16	0.12	0.04	0.02	0.02
$\rho_{\text{snow}}$ (kg m <sup>-3</sup> )	450.0	480.0	500.0	700.0	800.0
$\sigma_h$ (m)	0.0174	0.0174	0.0174	0.0174	0.0174
$l$ (m)	0.128	0.128	0.128	0.128	0.128

ues over the whole angular range, with the maximum contrast at the largest incidence angles.

At these snow wetness values (Table I), the signatures are expected to match late-spring scatterometer measurements that were previously made at 5.3 GHz over first-year ice. In fact, the *HH* polarized signatures shown in Fig. 10 closely resemble the radar-scattering cross sections acquired by Onstott [14] over multiyear ice in the Fram Strait in spring. This is not surprising since desalination and flushing by available snow meltwater had significantly reduced brine volumes in the surface layers of the Labrador Sea marginal ice. Circumstances therefore result in the reproduction of signatures from low salinity snow-covered sea ice.

#### B. Deformed Ice

The combined scattering model is tested for deformed ice regions using the assumption of a Gaussian distributed surface with a variable rms surface slope. As a guide and



Fig. 11. C-band SAR image of marginal sea ice off the east coast of Newfoundland, indicating low intensity regions of relatively undeformed ice, bright regions of deformed ice, and solitary, dark, saturated ice floes. The image was acquired and processed by the Canada Centre for Remote Sensing.

scaling factor, rms surface slopes and snow properties measured between March 16 and 26 are used to drive the predicted scattering response.

A C-band scattering signature from the LIMEX '87 experiment of March 13 was obtained prior to the surface observations recorded in Fig. 2(c) [47]. It is a mean scattering signature from a region of the MIZ derived by averaging the SAR image pixel intensities in the azimuthal direction, correcting for the antenna gain pattern, and then scaling the data to a relative backscattering coefficient ( $\sigma^0$  dB) using airborne C-band scatterometer backscatter cross-section measurements at an incidence angle of  $45^\circ$ . A signature is fitted to these data in Fig. 12 and the snow parameters necessary to generate this inverse model response are indicated. The closeness of fit to measured data is good, given actual surface conditions for that period. A 16-cm deep, low-density snow layer ( $\rho = 300 \text{ kg m}^{-3}$ ) with small grains (1.6-mm diam) and a low-volume fraction of liquid water (3 percent) are predicted and realistic given that cold weather and fresh snowfall preceded March 16 measurements. The other parameter of interest is the rms surface roughness of the surface, which is indicated as 0.4 rad ( $\sim 23^\circ$ ). This result indicates a reasonable degree of confidence in the model prediction. Evidently, marginal ice zone surface conditions did not change significantly over the three-day intervening period between the March 13 SAR and scatterometer measurements and surface characterization work. This lack of change in snow properties is consistent with temperatures that were predominantly below zero between March 13 and 15, although some metamorphism and increase in density is expected. A roughness prediction of rms slope  $s = 0.4$  rad is also consistent with the surface roughness conditions plotted in Fig. 9(a).

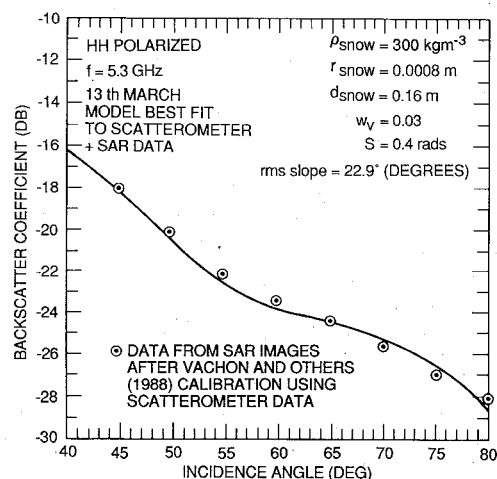


Fig. 12. Modeling fit to calibrated SAR data points extracted from an LIMEX '87 SAR image acquired on March 13. The snow parameters used to generate the fit are indicated.

Scattering signatures have been simulated for deformed ice using the combined Gaussian surface and volume-scattering model along with the rms slopes typical of sampled locations and snow parameters in Table I. It is evident from the results that signatures do not vary by more than 1 or 2 dB from those plotted in Fig. 10. It is suggested, therefore, that in order to generate observed radar contrasts between rough deformed and relatively smooth undeformed ice areas (Fig. 11), rough-surface snow and ice media must have either a much larger volume scatter component or a significantly rougher surface. These two alternatives provide the only valid explanation for the image contrasts observed in [46] between large undeformed floe surfaces and surrounding rougher ice.

Samples and field observations of surface roughness were limited to the locale of surface experiments. The CSS *Baffin* never penetrated more than several kilometers into the MIZ, and measurements did not capture more deformed regions of ice on SAR images further into the pack. Limited samples from uplifted and rafted blocks of ice in ridged portions of the pack support suggestions that these areas are better drained and more desalinated than floe surfaces. Containing less free water, such materials are more efficient volume scatterers than wet snow-covered floe surfaces. In addition, the MIZ underwent a severe ice compaction event which began on March 17 [37]. Between March 16 and 21, winds shifted from predominantly northeasterlies to southeasterlies (Fig. 2(a)). Rapid compaction took place, reducing the ice extent significantly (Fig. 1) and resulting in a high degree of rafting and pulverization of ice floes under the extreme pressure conditions. As a consequence, the areal proportion of deformed ice increased significantly. It is largely this factor which is expected to be the major cause of increasing  $\sigma^0$  values. Tilted blocks and floe edges exposed by rafting and pressure ridging contribute to higher rms slopes, and values of  $0.4 < s < 0.6$  are not expected to be uncommon. By March 25, under the influence of swell penetration, only an extremely small proportion of the ice floes

remained undeformed. Winds also changed, allowing the ice pressure to be relieved, and as waves fractured the ice into a discrete pack the discontinuous floe field no longer supported large piles of ice in rubble or ridges.

If the value of  $W_v$  in rubble or ridged ice is consistently lower by 0.02–0.04 and the surface becomes progressively more deformed, Fig. 13 shows simulated signatures for each day. Table II indicates the new parameters, showing the increase in the rms slope from 0.4 to 0.6 rad between March 16 and 21, during the ice compaction event. On subsequent days the rms slope used is  $s = 0.5$  because the effects of wave penetration and breakup had by this time fractured the MIZ into discrete floes, without components at the lower end of the roughness spectrum. Using this approach, it is predicted that the highest backscatter values over the range  $40^\circ < \theta < 80^\circ$  occurs on March 21st. Only on March 25 and 26 do the values of  $\sigma^0$  exceed those of the 21st, between  $40^\circ$  and  $50^\circ$  incidence. The explanation for the higher gradient in the case of the last two days is the same as in Fig. 10 and is due to the increasing water content and snow depth.

It was clear during the LIMEX '87 operations that ice-pressure conditions reached a peak on March 21st. This severe compaction event is explained by the winds in Fig. 2(a) shifting to predominantly southeasterlies and herding ice towards the shore. It is expected from the model results, therefore, that regions of deformed ice in SAR images increase in brightness over this period. One method of extracting quantitative information from uncalibrated SAR images is to investigate the statistics of digital number (DN) values corresponding to pixel intensities. Using these data, it is possible to validate the model observations. Recorded DN values from LIMEX SAR images such as Fig. 11 are related to the backscatter cross section of the surface [48], with the value of  $DN^2$  directly proportional to  $\sigma^0$ . Digital numbers may be compared within a scene provided that the system has a good relative calibration. The reliability of relative calibration over a period of several days is low due to drift in the system parameters and variations in instrument gain, and it is safer to investigate relative intensities within a single scene. Digby Argus and Carsey [46] extracted DN values from regions of deformed and undeformed ice (in areas with large distinct floes surrounded by brighter material) by using two scenes of the same region. For March 18 they calculate statistics for the DN values obtained from floes in the Cape Freels region and their surrounding pack; then by using an image of the same region on March 21 have identified the same floes and have calculated similar statistics. The result is that the relative contrast between the two surface roughness classes on March 18 is low; the difference between the mean DN value is 2 and the standard deviation of both surfaces is 18. By March 21, DN statistics have changed somewhat and the relative contrast between the floes and their surroundings increases. The difference between the mean DN values of both floe and surroundings has increased to 31, while the standard de-

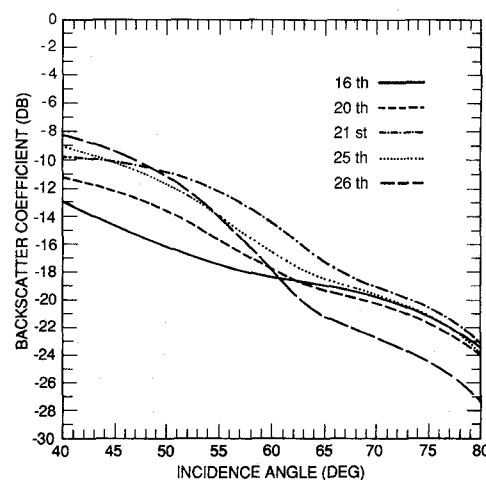


Fig. 13. Simulated C-band HH polarized scattering signatures for a deformed, Gaussian distributed sea-ice surface on each of the five days, using parameters listed in Table II.

TABLE II  
PARAMETERS USED IN MODELING DEFORMED ICE SIGNATURES BETWEEN MARCH 16–26

Snow Property	16/03	20/03	21/03	25/03	26/03
$r_{\text{snow}}$ (m)	0.001	0.0011	0.00125	0.00125	0.00125
$W_v$	0.03	0.05	0.07	0.07	0.11
$d_{\text{snow}}$ (m)	0.16	0.12	0.04	0.02	0.02
$\rho_{\text{snow}}$ (kg m <sup>-3</sup> )	450.0	480.0	500.0	700.0	800.0
$s$ (rad)	0.4	0.5	0.6	0.5	0.5

viation of both areas increases to 22 and 27, respectively [46]. These changes in image characteristics are attributed to the increase in surface wetness as temperatures rise, and such increases in the image contrast are evident in various imaged locations in the MIZ on these days.

In Fig. 14 the relative backscatter contrast between deformed and undeformed ice has been calculated using the pairs of curves for each date in Figs. 10 and 13. This exercise is designed to see if the increase in contrast between rough and smooth surfaces is reproduced by the model from March 16–21. Resulting curves demonstrate that the distinction between simulated signatures for these broad roughness classes is least on March 16, with a minimum contrast of 1 dB at  $\theta = 55^\circ$ . The mean angular contrast increases on March 20 and reaches an expected maximum on March 21 of 3.5 dB. Peak radar backscatter contrast between deformed ice and undeformed snow-covered floes is approximately 5 dB and occurs for  $45^\circ < \theta < 60^\circ$ . The predicted backscatter contrast between the deformed ice on March 21 (Fig. 13) and the saturated surface in Fig. 10 is also calculated for comparison. In cases where deformed ice surrounds smooth floes with saturated surfaces, the contrast may be expected to in-

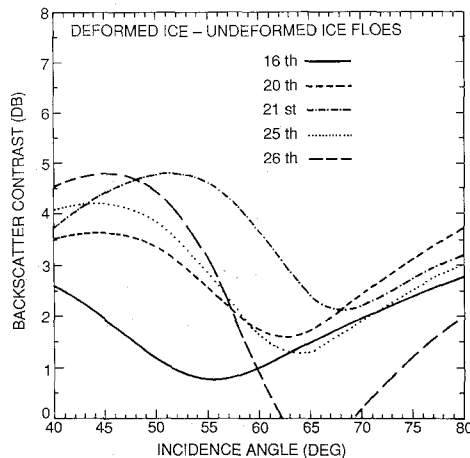


Fig. 14. Predicted radar backscatter contrast between deformed and undeformed ice signatures on each of the experiment days, using parameters listed in Tables I and II, and Gaussian and exponential surface correlation assumptions, respectively.

crease from 7 dB at 40° to 19 dB at 80°. After March 21, reduced rms slopes interestingly do not have much effect upon contrast in the 40°–55° incidence angle range, although at larger incidence angles the contrast is reduced by several dB. In the case of March 26, the predicted contrast reverses slightly between 62° and 69°.

### VIII. CONCLUSIONS AND DISCUSSION

Surface characterization work during LIMEX '87 gives an important insight into the major processes at work in the snow and ice surface layers during the onset of melt. A simple combined model demonstrates the effect of a variety of surface parameters observed during LIMEX '87 upon 5.3-GHz two-dimensional radar backscatter signatures. It is evident that the major factors modulating scattering characteristics are the degree of snow metamorphosis, surface wetness, and large-scale surface roughness. When a damp snow cover is present, the C-band signature is largely a response to snow parameters rather than the ice beneath. Examples demonstrate that even shallow damp snow masks the scattering response contribution from the first-year ice surface because of attenuation or extinction in a wet snow layer. In certain cases, when the snow cover is melted, the scattering response is controlled by the degree of desalination of first-year ice and the scale of roughness of the surface. Saturated or ponded floes cause a specular response and result in the steepest gradients of  $\sigma^0$  over the 40° <  $\theta$  < 80° range. The consequence is a high degree of contrast between such wet floes and their surroundings, which is readily observed in the SAR images.

The model presented here can be used to demonstrate the contrasting scattering circumstances observed during the course of LIMEX '87. It can also predict relative differences in  $\sigma^0$  between specific ground targets in order to make comparisons with image properties. Results indicate the possibility of identifying areas of deformed and undeformed ice at a time of year when signature varia-

tions due to ice typology are suppressed by snow moisture. This work indicates that the SAR may be used more efficiently during the spring/summer melt period to measure variations in the spatial extent of such classes of ice, and using this information make progress towards inferring the thickness distribution of the ice.

LIMEX '87 encountered a specific range of melt and pressure ice conditions which lend themselves well to the use of this simplified combined backscatter model. A further experiment (LIMEX '89) which took place in March 1989 provided a new, extended *in situ* dataset under a contrasting range of conditions and enable such models to be enhanced. Improvements to the CCRS C-band SAR instrument ensured that a fully calibrated coincident digital SAR dataset was acquired with which to test and validate models and to provide fresh insight into the range of scattering signatures encountered in the Labrador Sea under early-melt conditions.

### ACKNOWLEDGMENT

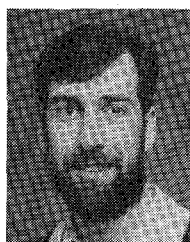
The author thanks B. Holt and F. Carsey (Jet Propulsion Laboratory) and the reviewers for their valuable comments, and for the way in which LIMEX '87 participants freely circulated data. Additional helpful suggestions about the manuscript were made by G. Rees, V. Squire, and D. Winebrenner.

### REFERENCES

- [1] L. McNutt *et al.*, "LIMEX '87: The Labrador Ice Margin Experiment, March 1987—A pilot experiment in anticipation of RADARSAT and ERS 1 data," *EOS*, vol. 69, no. 23, p. 634, 1988.
- [2] M. R. Drinkwater and S. Digby Argus, "LIMEX '87: An international experiment in the Labrador sea marginal ice zone," *Polar Rec.*, to be published.
- [3] S. K. Parashar, "Investigation of radar discrimination of sea ice," Ph.D. thesis, University of Kansas, Lawrence, 1974.
- [4] R. G. Onstott, R. K. Moore, and W. F. Weeks, "Surface-based scatterometer results of Arctic sea ice," *IEEE Trans. Geosci. Remote Sensing*, vol. GE-17, no. 3, pp. 78–85, 1979.
- [5] R. G. Onstott, R. K. Moore, S. Gogineni, and C. Delker, "Four years of low-altitude broadband backscatter measurements," *IEEE J. Oceanic Eng.*, vol. OE-7, no. 1, pp. 44–50, 1982.
- [6] A. L. Gray, R. K. Hawkins, C. E. Livingstone, L. D. Arsenault, and W. M. Johnstone, "Simultaneous scatterometer and radiometer measurements of sea ice microwave signatures," *IEEE J. Oceanic Eng.*, vol. OE-7, no. 1, pp. 20–32, 1982.
- [7] C. E. Livingstone, R. G. Onstott, L. D. Arsenault, A. L. Gray, and K. P. Singh, "Microwave signatures near the onset of melt," *IEEE Trans. Geosci. Remote Sensing*, vol. GE-25, no. 2, pp. 174–187, 1987.
- [8] A. K. Fung and H. J. Eom, "Application of a combined rough surface and volume scattering theory to sea ice and snow backscatter," *IEEE Trans. Geosci. Remote Sensing*, vol. GE-20, no. 4, pp. 528–536, 1982.
- [9] Y. S. Kim, "Theoretical and experimental study radar backscatter from sea ice," Ph.D. thesis, University of Kansas, Lawrence, 1984, 168pp.
- [10] Y. S. Kim, R. K. Moore, R. G. Onstott, and S. Gogineni, "Towards identification of optimum radar parameters for sea ice monitoring," *J. Glaciol.*, vol. 31, no. 109, pp. 214–219, 1985.
- [11] R. G. Onstott, "Theoretical and experimental study of the backscatter of Arctic sea ice," in *Proc. IGARSS'87 Symp.* (Ann Arbor, MI), May 18–21, 1987, pp. 1127–1130.
- [12] M. R. Drinkwater, "Radar altimetric studies of polar ice," Ph.D. thesis, University of Cambridge, Cambridge, Eng., 1988, 231pp.
- [13] M. R. Drinkwater and G. B. Crocker, "Modelling changes in the dielectric and scattering properties of young snow-covered sea ice at GHz frequencies," *J. Glaciol.*, vol. 34, no. 118, pp. 274–282, 1988.

- [14] R. G. Onstott, T. C. Grenfell, C. Mätzler, C. A. Luther, and E. A. Svendsen, "Evolution of microwave sea ice signatures during early summer and midsummer in the marginal ice zone," *J. Geophys. Res.*, vol. 92, no. C7, pp. 6825-6835, 1987.
- [15] E. B. Jones, "Snowpack ground-truth manual," Resource Consultants, Inc., Fort Collins, CO, NASA Contract Rep. 170584, 1983, 41pp.
- [16] R. G. Stone, "The classification, nomenclature, and definitions of the forms of ice and snow according to Seligman," *Bull. Amer. Meteorol. Soc.*, pp. 47-53, Jan. 1937.
- [17] B. Holt and S. A. Digby, "Processes and imagery of first-year fast sea ice during the melt season," *J. Geophys. Res.*, vol. 90, no. C3, pp. 5045-5062, 1985.
- [18] W. F. Weeks and S. F. Ackley, "The growth, structure and properties of sea ice," U.S. Army Cold Regions Res. and Eng. Lab., Hanover, NH, Mono. 82-1, 1982, 130pp.
- [19] N. Untersteiner, "Natural desalination and equilibrium salinity profile of perennial sea ice," *J. Geophys. Res.*, vol. 73, no. 4, pp. 1251-1257, 1968.
- [20] S. C. Colbeck, "The geometry and permittivity of wet snow at high frequencies," *J. Appl. Phys.*, vol. 53, no. 6, pp. 4495-4500, 1982.
- [21] M. T. Tiuri, A. H. Sihvola, E. G. Nyfors, and M. T. Hallikainen, "The complex dielectric constant of snow at microwave frequencies," *IEEE J. Oceanic Eng.*, vol. OE-9, no. 5, pp. 377-382, 1984.
- [22] M. T. Hallikainen, M. V. O. Toikka, and J. M. Hyypä, "Microwave dielectric properties of low-salinity sea ice" in *Proc. IGARSS '88 Symp.* (Edinburgh, Scotland), Sept. 13-16, 1988, pp. 419-420.
- [23] C. Mätzler, H. Aebischer, and E. Schanda, "Microwave dielectric properties of surface snow," *IEEE J. Oceanic Eng.*, vol. OE-9, no. 5, pp. 366-371, 1984.
- [24] H. W. Loeb, G. M. Young, P. A. Quickenden, and A. Suggett, "New methods for measurement of complex permittivity up to 13 GHz and their application to the study of dielectric relaxation of polar liquids including aqueous solutions," *Ber. Bunsenges. Phys. Chem.*, vol. 75, no. 11, pp. 1155-1164, 1971.
- [25] L. S. Taylor, "Dielectric properties of mixtures," *IEEE Trans. Antennas Propagat.*, vol. AP-13, no. 6, pp. 943-947, 1965.
- [26] T. Grenfell, "Determination of the liquid water content of snow by the dye dilution technique," *Cold Regions Sci. and Tech.*, vol. 12, pp. 295-298, 1986.
- [27] Y. S. Kim, R. G. Onstott, and R. K. Moore, "The effect of a snow cover on microwave backscatter from sea ice," *IEEE J. Oceanic Eng.*, vol. OE-9, no. 5, pp. 383-388, 1984.
- [28] M. R. Vant, R. O. Ramseier, and V. Makios, "The complex dielectric constant of sea ice at frequencies in the range 0.1-40 GHz," *J. Appl. Phys.*, vol. 49, no. 3, pp. 1264-1280, 1978.
- [29] S. A. Arcone, A. J. Gow, and S. McGrew, "Structure and dielectric properties at 4.8 and 9.5 GHz of saline ice," *J. Geophys. Res.*, vol. 91, no. C12, pp. 14281-14303, 1986.
- [30] F. T. Ulaby, W. H. Stiles, and M. Abdelrazik, "Snowcover influence on backscattering from terrain," *IEEE Trans. Geosci. Remote Sensing*, vol. GE-22, no. 2, pp. 126-132, 1984.
- [31] A. Assur, "Composition of sea ice and its tensile strength," SIPRE, Res. Rep. no. 44, 1960.
- [32] G. Poe, A. Stogryn, and A. T. Edgerton, "A study of the microwave emission characteristics of sea ice," Aerojet Electrosystems Co., Azusa, CA, Final Tech. Rep. 1749R-2, 1972, 89pp.
- [33] G. Frankenstein and R. Garner, "Equations for determining the brine volume of sea ice from  $-0.5^{\circ}\text{C}$  to  $-22.9^{\circ}\text{C}$ ," *J. Glaciol.*, vol. 6, no. 48, pp. 943-944, 1967.
- [34] W. H. Stiles and F. W. Ulaby, "The active and passive microwave response to snow parameters: 1. Wetness," *J. Geophys. Res.*, vol. 85, vol. C2, pp. 1037-1044, 1980.
- [35] M. Suzuki, T. Matsumoto, D. Kuroiwa, K. Fujino, and G. Wakahama, "Research on the interaction of microwaves with snow and ice: Part 1. A study on the microwave backscattering from a melting snowpack," *Mem. Nat. Instit. Polar Res.*, no. 29 (special issue), pp. 166-175, 1983.
- [36] F. W. Ulaby, R. K. Moore, and A. K. Fung, *Microwave Remote Sensing Active and Passive*. Reading, MA: Addison-Wesley, 1982, pp. 457-1064.
- [37] F. D. Carsey and S. Digby Argus, "Use of SAR imagery and other remotely-sensed data in deriving ice information during a severe ice event on the Grand Banks" in *Proc. IGARSS '88 Symp.* (Edinburgh, Scotland), Sept. 12-16, 1988, pp. 1431-1434.
- [38] H. J. Eom, "Theoretical scatter and emission models for microwave remote sensing," Ph.D. thesis, University of Kansas, Lawrence, 1982, 212pp.
- [39] D. E. Barrick, "Rough surface scattering based on the specular point theory," *IEEE Trans. Antennas Propagat.*, vol. AP-16, no. 4, pp. 449-454, 1968.
- [40] A. K. Fung and H. L. Chan, "Backscattering of waves by composite rough surfaces," *IEEE Trans. Antennas Propagat.*, vol. AP-17, no. 5, pp. 590-598, 1969.
- [41] A. K. Fung, "A review of surface scatter theories for modelling applications" in *Coherent and Incoherent Radar Scattering from Rough Surfaces and Vegetated Areas (Proc. ESA-EARSeL Workshop, Alpbach, Mar. 16-20, 1981)*, ESA Sci. and Tech. Pubs. Branch, Noordwijk, The Netherlands, ESA SP-166, pp. 71-82.
- [42] S. T. Wu and A. K. Fung, "A non-coherent model for microwave emissions and backscattering from the sea surface," *J. Geophys. Res.*, vol. 77, no. 30, pp. 5917-5929, 1972.
- [43] T. Mo, J. R. Wang, and T. J. Schmugge, "Estimation of surface roughness parameters from dual-frequency measurements of radar backscattering coefficients," *IEEE Trans. Geosci. Remote Sensing*, vol. 26, no. 5, pp. 574-579, 1988.
- [44] H. C. Van de Hulst, *Light Scattering by Small Particles*. New York: Wiley, 1957.
- [45] D. E. Kerr, *The Propagation of Short Radio Waves* (MIT Radiation Lab Series, no. 13). New York: McGraw-Hill, 1951.
- [46] S. Digby Argus and F. D. Carsey, "SAR imagery of the Grand Banks ice pack and its relationship to surface features" in *Proc. IGARSS '88 Symp.* (Edinburgh, Scotland), Sept. 12-16, 1988, pp. 1425-1428.
- [47] P. W. Vachon, R. B. Olsen, C. E. Livingstone, and N. G. Freeman, "Airborne SAR imagery of ocean surface waves obtained during LEWEX: Some initial results," *IEEE Trans. Geosci. Remote Sensing*, vol. 26, no. 5, pp. 548-561, 1988.
- [48] C. E. Livingstone et al., "CCRS C-band airborne radar—system description and test results," paper presented at the 11th Can. Symp. on Remote Sensing, Waterloo, ON, June 22-25, 1987.

\*



**Mark R. Drinkwater** received the B.Sc. (Hons.) degree in geography from Durham University, Durham, Eng., in 1984, specializing in remote sensing and glaciology, and the Ph.D. degree in radar remote sensing of polar ice from the Scott Polar Research Institute and Emmanuel College of the University of Cambridge, Cambridge, Eng., in 1988.

He worked as a Research Scientist for Polar Oceans Associates, a U.K. division of Science Applications, Inc. of San Diego, CA, before joining the Jet Propulsion Laboratory, California Institute of Technology, Pasadena, as a Resident Research Associate, where he has pursued techniques in modeling microwave backscatter properties of snow and ice media. His current research interests as a member of the Polar Oceanography Group include multifrequency polarimetric microwave observations of the marginal ice zone and terrestrial ice sheets.

Dr. Drinkwater is a member of the International Glaciological Society and the U.K. Remote Sensing Society.